Energy Engineering

Tech Science Press

DOI: 10.32604/ee.2024.054687

ARTICLE

Heuristic-Based Optimal Load Frequency Control with Offsite Backup Controllers in Interconnected Microgrids

Aijia Ding and Tingzhang Liu*

School of Mechatronic Engineering and Automation, Shanghai University, Shanghai, 200444, China

*Corresponding Author: Tingzhang Liu. Email: liutzhcom@oa.shu.edu.cn

Received: 05 June 2024 Accepted: 18 August 2024 Published: 22 November 2024

ABSTRACT

The primary factor contributing to frequency instability in microgrids is the inherent intermittency of renewable energy sources. This paper introduces novel dual-backup controllers utilizing advanced fractional order proportional integral derivative (FOPID) controllers to enhance frequency and tie-line power stability in microgrids amid increasing renewable energy integration. To improve load frequency control, the proposed controllers are applied to a two-area interconnected microgrid system incorporating diverse energy sources, such as wind turbines, photovoltaic cells, diesel generators, and various storage technologies. A novel meta-heuristic algorithm is adopted to select the optimal parameters of the proposed controllers. The efficacy of the advanced FOPID controllers is demonstrated through comparative analyses against traditional proportional integral derivative (PID) and FOPID controllers, showcasing superior performance in managing system fluctuations. The optimization algorithm is also evaluated against other artificial intelligent methods for parameter optimization, affirming the proposed solution's efficiency. The robustness of the intelligent controllers against system uncertainties is further validated under extensive power disturbances, proving their capability to maintain grid stability. The dual-controller configuration ensures redundancy, allowing them to operate as mutual backups, enhancing system reliability. This research underlines the importance of sophisticated control strategies for future-proofing microgrid operations against the backdrop of evolving energy landscapes.

KEYWORDS

Fractional order PID; interconnected microgrids; load frequency control; meta-heuristic algorithm; parameter optimization

1 Introduction

The integration of intermittent renewable energy and the proliferation of electric vehicles (EV) has reduced system inertia, intensifying the challenges associated with grid stability, particularly in frequency and tie-line power flow management [1]. Historical approaches to this dilemma have seen the development of various strategies within multi-area interconnected power systems aimed at fortifying frequency stability [2], including the utilization of tilt-integral-derivative (TID) controller [3,4], integration of controller gain optimization and anti-windup augmentation [5], the deployment of robust H_2/H_∞ controllers [6], inertia-adaptive model predictive control [7], virtual inertia emulation [8], and fuzzy logic control [9]. The TID controller exemplifies the adaptable modulation of closed-loop parameters, robust performance, and enhanced disturbance attenuation capabilities. Dragonfly search-based (1 + PD)-PID cascade controller is designed to address the load frequency control

[10]. However, only step load perturbation is considered to validate the controller performance and the robustness of the method is not assessed. Cohort Intelligence (CI) optimization-based FOPID is adopted to tune the parameters achieving better steady-state precision than genetic algorithm and particle swarm optimization tuned PID controllers [11]. To settle the system stability issue facing higher penetration of renewable energy and EV charging/discharging power in interconnected microgrids, Harris hawks optimization (HHO) based method is proposed to tune the integral gains for EV charging/discharging power [12]. Two-layer multiple model predictive controller (TLMMPC) is developed to determine the output power of the energy storage system (ESS) in ESS integrated microgrid [13].

Among these, fractional order PID (FOPID) controllers also have distinguished themselves, recognized for their robust performance, reduced steady-state error, and formidable disturbance rejection capabilities, particularly in load frequency control (LFC) scenarios [14]. The effectiveness of FOPID controllers is dependent on the fine-tuning of the λ and μ parameters in conjunction with the conventional proportional (k_P), integral (k_I), and derivative (k_D) coefficients [14]. A Cascaded FOPID-tilt integrator differentiator with filter (TIDF) based on Manta-Ray Foraging Optimization is proposed in [15]. Besides, a cascaded proportional integral-tilt integral derivative (PI-TID) controller with parameters optimized utilizing chaotic butterfly optimization (CBO) was proposed in [16]. Reference [17] combined TID controller and Harris hawks optimization optimization (HHO) to obtain better performance than PID and PI controllers. Despite their advantages, the fine-tuning of these parameters remains challenging due to microgrids' intrinsic non-linearity and uncertainty owing to evolving lifestyle patterns, escalating energy consumption, industrial advancement, ecological considerations, and advancements in power grid infrastructure [18]. Addressing this challenge of optimum parameters, other meta-heuristic optimization techniques, including Kharitonov's theorem applications [19] and Gases Brownian Motion Optimization (GBMO) [20], have been proposed, albeit at the cost of increased computational complexity.

This research examines a two-area interconnected microgrid system incorporating diverse intermittent renewable resources such as wind turbine generators (WG), solar photovoltaics (PV), diesel generators (DsG), fuel cells (FC), flywheel storage systems (FWSS), and battery energy storage system (BESS). We introduce two innovative structures of FOPID controller designs—FOPID cascaded with fractional-order PI (FOPID-C-FOPI) and parallel fractional-order PI (FOPID-P-FOPI)—to advance the LFC responsiveness and flexibility. These designs exceed the disturbance rejection and robustness of conventional PID [21] and FOPID controllers. The novel controllers are fine-tuned using a Heap-Based Optimization (HBO) algorithm [22], which optimizes the hierarchical decision-making characteristic of corporate structures, enhancing efficiency in problem-solving.

In this structured approach, we explore the foundational concepts of HBO, delineate the system model, articulate the optimization challenges, and discuss controller design and implementation. This optimization method allows the proposed controllers to operate as mutual backups, enhancing system reliability under various oscillations.

The paper progresses with a comprehensive system model in Section 2, an exposition of the optimization challenges and controller strategies in Section 3, and a detailed analysis of simulation outcomes in Section 4. Section 5 concludes the paper with a synopsis of key findings and their implications for future system operation and research.

2 Model Formulation

This study investigates a dual-area Microgrid (MG) network, each encompassing DsG, FC, WG, PV, FWSS, and BESS. Fig. 1 illustrates the control architecture of the interconnected MGs.

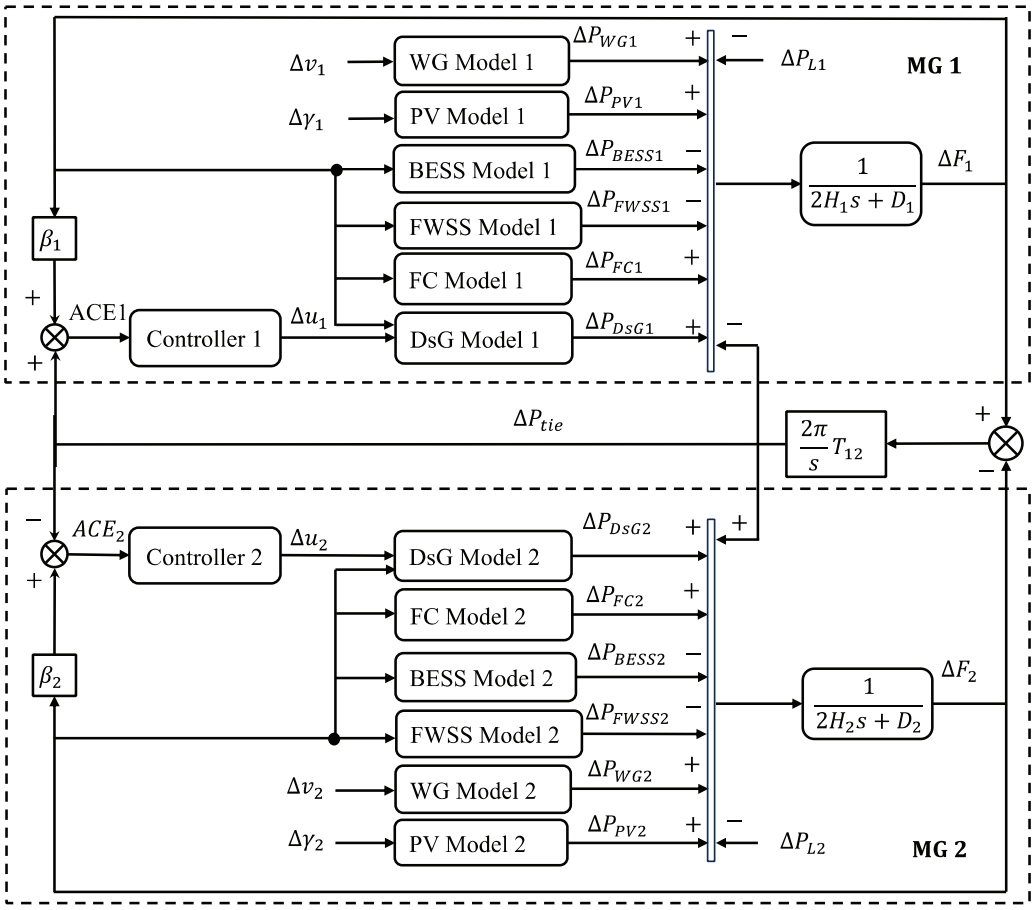

Figure 1: Control diagram of the interconnected system

Control signals, Δu_1 and Δu_2, emitted by two structurally identical but parameter-differentiated controllers, are predicated on the area control error (ACE) of each MG, denoted as ACE_1 and ACE_2. The ACE_i is formulated in Eq. (1), incorporating the bias coefficient β_i, the frequency deviation in MG_i, ΔF_i, and the tie-line power deviation $\Delta P_{tie,ij}$ from Eq. (2), with T_{ij} representing the inter-area synchronous torque coefficient.

$$ACE_i = \Delta P_{tie,i} + \beta_i \Delta F_i \tag{1}$$

$$\Delta P_{tie,ij}(s) = 2\pi T_{ij}\left(\Delta F_i(s) - \Delta F_j(s)\right)/s \tag{2}$$

System variations encompass wind generation changes (ΔP_{WG}), photovoltaic output fluctuations (ΔP_{PV}), and load disturbances (ΔP_L), influenced by wind speed (Δv) and solar irradiance ($\Delta \gamma$) variations. Inertia (H_i) and damping coefficients (D_i) within each area contribute to system dynamics.

The subsequent sections provide an academic outline of various renewable and storage systems within an MG. They are structured sequentially concerning their functions, dynamic models, and roles within the broader MG control context.

2.1 Diesel Generator (DsG) Dynamics

DsG units are pivotal in isolated MG systems, offering fast start-up, high efficiency, and long service life. They dynamically balance power supply to mitigate perturbations and renewable source fluctuations, critical for transient response enhancement [23,24]. The DsG model, a first-order representation including governor and turbine dynamics [25], encapsulates power adjustments in response to frequency variations in Eq. (3).

$$G_{dg}(s) = -\frac{1}{R_{dsg}\left(T_g s+1\right)\left(T_{tg} s+1\right)} \tag{3}$$

where T_g and T_{tg} are presented separately as governor time constant and turbine time constant. R_{dsg} is the droop coefficient of the DsG unit.

Derived from first-order governor and generator models, the dynamic DsG model incorporates ramp rate and power output constraints under saturation conditions. Fig. 2 demonstrates the model input as frequency deviation (ΔF) with the LFC signal (Δu) treated as a perturbation. Ramp rate ($\pm\delta_g$) and power output limitations (μ_g) are established through saturation parameters $Saturation_{g1}$ and $Saturation_{g2}$, respectively. The output response of the DsG model, ΔP_{DsG}, signifies the regulation action: a zero value indicates equilibrium, positive values indicate demand surpassing supply, and negative values indicate the converse. The DsG's critical involvement in primary frequency control (PFC) and LFC underscores its integral role in system stability.

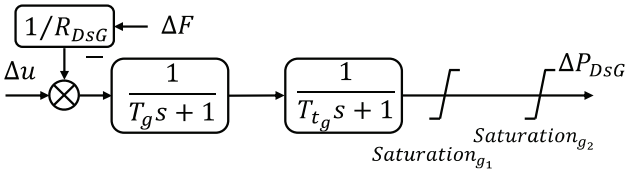

Figure 2: Dynamic model of DsG unit

2.2 Fuel Cell (FC) Unit Dynamics

FC units contribute to power equilibrium by converting chemical to electrical energy using eco-friendly hydrogen and oxygen [26]. The FC dynamics are represented by a third-order transfer function in Eq. (4), capturing the system's time constants and responsiveness to control signals from LFC.

$$G_{fc}(s) = -\frac{1}{\left(T_{fc} s+1\right)\left(T_{in_{fc}} s+1\right)\left(T_{ic_{fc}} s+1\right)} \tag{4}$$

where $T_{in_{fc}}$ and $T_{ic_{fc}}$ represent the time constants for the inverter and interconnection device, respectively, while T_{fc} corresponds to the FC unit time constant. The model receives the LFC signal, Δu, originating from the ACE-influenced controller, to regulate the FC power output ΔP_{FC}. Fig. 3 depicts the third-order dynamic behavior of the FC unit, where $Saturation_{fc_1}$ specifies the ramp rate constraint ($\pm\delta_{fc}$) and $Saturation_{fc_2}$ indicates the power output ceiling (μ_{fc}). The FC's sole function within the LFC mechanism is highlighted in Fig. 3.

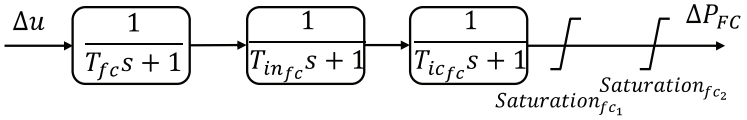

Figure 3: Dynamic model of FC. Adapted from Refenence [27]

2.3 Energy Storage Systems Dynamics

Battery energy storage system (BESS) and flywheel storage system (FWSS) are modeled as first-order systems in Eqs. (5) and (6), which are crucial for PFC by absorbing and dispatching energy in response to frequency deviations. Both are modeled to provide only PFC, with their dynamics solely responsive to local frequency variations (ΔF). Exhibited in Fig. 4, their first-order transfer functions, denoted as $G_b(s)$ and $G_{fw}(s)$, are expressed in Eqs. (5) and (6), with T_b and T_{fw} representing the time constants of BESS and FWSS, respectively.

$$G_b(s) = 1/(T_b s + 1) \tag{5}$$

$$G_{fw}(s) = 1/\left(T_{fw} s + 1\right) \tag{6}$$

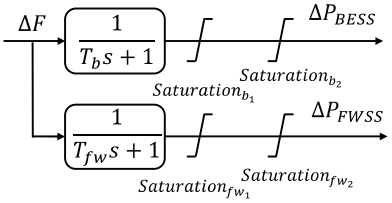

Figure 4: Dynamic model of BESS and FWSS. Reprinted from Reference [28]

These models produce power fluctuations (ΔP_{BESS}, ΔP_{FWSS}) as outputs in response to the input frequency changes. Constraints on the ramp rates ($\pm\delta_b$ for BESS as $Saturation_{b_1}$, $\pm\delta_{fw}$ for FWSS as $Saturation_{fw_1}$) and output power limits ($\pm\mu_b$ for BESS as $Saturation_{b_2}$, $\pm\mu_{fw}$ for FWSS as $Saturation_{fw_2}$) are imposed to simulate operational limits, as shown in Fig. 4.

2.4 Photovoltaic (PV) Model

PV units, devoid of mechanical inertia, rely on solar irradiance changes to modulate power output. The photovoltaic (PV) system model takes the variation of solar irradiation ($\Delta\gamma$) as its input, which diverges from the traditional second-order models referenced in [29] by incorporating additional dynamics. The resulting PV power output variation (ΔP_{PV}) is governed by a third-order transfer function, $G_{pv}(s)$, represented in Eq. (7) [25], underscoring the inverter and interconnection dynamics and their role in power generation responsiveness.

$$G_{pv}(s) = -\frac{1}{\left(T_{pv} s + 1\right)\left(T_{in_{pv}} s + 1\right)\left(T_{ic_{pv}} s + 1\right)} \tag{7}$$

where $T_{in_{pv}}$ and $T_{ic_{pv}}$ denote the time constants of the inverter and interconnection device within the PV system, respectively, while T_{pv} is the time constant of the PV unit itself. This advanced model for the PV system, akin to that of the fuel cell unit, is depicted in Fig. 5 and enables refined control for LFC.

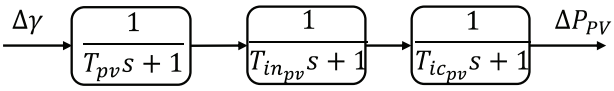

Figure 5: Dynamic model of PV

2.5 Wind Generator (WG) Model

WG systems, inherently non-dispatchable, are characterized by a first-order transfer function in Eq. (8). The model relies on wind speed variations to predict power output changes, highlighting the WG's responsive nature to environmental conditions [30].

$$G_{wg}(s) = 1/\left(T_{wg}s + 1\right) \tag{8}$$

where T_{wg} is the time constant of WG. This model processes wind speed variations (Δv) as input to yield the corresponding power output variations (ΔP_{WG}), encapsulated in the transfer function illustrated in Fig. 6.

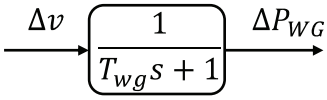

Figure 6: Dynamic model of WG

3 Problem Formulation

The optimization framework prioritizes an objective function to minimize frequency fluctuations and concurrent tie-line power imbalances. Within this construct, innovative controller configurations, specifically the FOPID-C-FOPI and FOPID-P-FOPI, are integrated into the LFC loop to formulate control directives for DsG. The calibration of these novel controllers leverages the advanced HBO algorithm to refine their parameters for optimal performance.

3.1 Objective Function

LFC aims to mitigate deviations in system frequency and tie-line power. Accordingly, the optimization target is formulated as an integral time-multiplied absolute error (ITAE) metric, quantified in Eq. (9) to evaluate performance deviations over time.

$$\text{ITAE} = \int_{t_0}^{t_{final}} \left(|\Delta F_1| + |\Delta F_2| + |\Delta P_{tie}|\right) t dt \tag{9}$$

Utilizing the ITAE index, the optimization problem aims to minimize the ITAE value, subject to constraints delineated in Eqs. (10)–(14):

$$k_{P_{min}} \le k_{P_{ij}} \le k_{P_{max}} i, j = 1, 2 \tag{10}$$

$$k_{I_{min}} \le k_{I_{ij}} \le k_{I_{max}} i, j = 1, 2 \tag{11}$$

$$k_{D_{min}} \le k_{D_i} \le k_{D_{max}} i = 1, 2 \tag{12}$$

$$\lambda_{min} \le \lambda_{ij} \le \lambda_{max} i, j = 1, 2 \tag{13}$$

$$\mu_{min} \leq \mu_i \leq \mu_{max} i = 1, 2 \tag{14}$$

where $k_{P_{ij}}$, $k_{I_{ij}}$, and k_{D_i} represent the proportional, integral, and differential gains, respectively, while λ_{ij} and μ_i denote the fractional orders of integration and differentiation. These parameters are non-negative real numbers, with upper and lower bounds specified in Eqs. (10)–(14). The ITAE is employed as the fitness function for optimization, using the HBO method to determine the optimal settings for the controllers. For uniformity, parameters across the two interconnected areas are kept consistent, barring differences in the LFC controllers.

3.2 Controller Design

To mitigate frequency and tie-line power deviations stemming from renewable energy variability and load disturbances, advanced PID variants such as the Tilt-Integral-Derivative (TID) controller [3] and the Integral-Derivative-Tilted (ID-T) controller [4] were developed. These approaches address the complexities introduced by the proportional gain substitution $k_P/s^{1/n}$ (where n is the tilt fractional component ranging between [1,10]). Consequently, the FOPID-C-FOPI controller, depicted in Fig. 7 and influenced by [31,32], simplifies the computational process. This controller incorporates the fractional order operator ${}_aD_t^{\alpha}$, providing a more robust framework for controlling dynamic system responses. ${}_aD_t^{\alpha}$ is denoted as Eq. (15):

$${}_aD_t^{\alpha} = \begin{cases} d\alpha/\mathrm{d}t^{\alpha}, R(\alpha) > 0 \\ 1, R(\alpha) = 0 \\ \int_0^t (d\tau)^{\alpha}, R(\alpha) < 0 \end{cases} \tag{15}$$

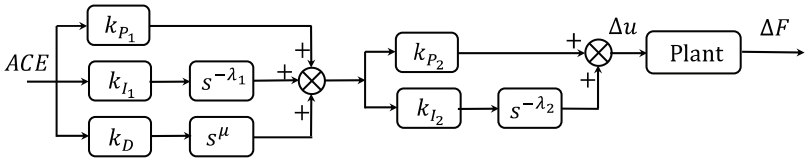

Figure 7: FOPID cascaded FOPI

Various methodologies for fractional order derivatives and integrals have been developed, including the Grunwald–Letnikov, Riemann–Liouville (RL), and Caputo definitions, alongside the Carlson and Matsuda approximations [33]. Notably, the Riemann–Liouville definition is frequently employed for fractional derivatives, as specified in Eq. (16) [34]:

$${}_aD_t^{\alpha} f(t) = \frac{1}{\Gamma(n-\alpha)} \frac{d^n}{dt^n} \int_a^t (t-\tau)^{n-\alpha-1} f(\tau)\, d\tau \tag{16}$$

where $n-1 \leq \alpha < n$, n is an integer number, and $\Gamma(\cdot)$ is Euler's gamma function. The fractional integral is given in Eq. (17):

$${}_aD_t^{\alpha} f(t) = \frac{1}{\Gamma(\alpha)} \int_a^t (t-\tau)^{\alpha-1} f(\tau)\, d\tau \tag{17}$$

The Laplace transform is extensively employed to represent both fractional and integer order differentiations. Typically, for a fractional order α where $0 < \alpha < 1$, the Laplace transform of the

Riemann-Liouville fractional derivative or integral is defined in Eq. (18):

$$L\left\{{}_aD_t^{\alpha}f\left(t\right)\right\} = s^{\alpha}F\left(s\right) - \sum_{k=0}^{n-1} s^{k}\,{}_aD_t^{\alpha-k-1}f\left(t\right)|_{t=0} \tag{18}$$

Under zero initial conditions for $n-1 \le \alpha < n$, the Laplace transform is shown in Eq. (19):

$$L\left\{{}_aD_t^{\pm\alpha}f\left(t\right)\right\} = s^{\pm\alpha}F\left(s\right) \tag{19}$$

where $L\{\cdot\}$ represents the Laplace transform, indicating that for dynamic systems described by differential equations with fractional derivatives and assumed zero initial conditions, the resultant transfer functions are characterized by fractional-order s.

The transfer function for the proposed FOPID-C-FOPI controller is defined in Eq. (20):

$$G_{FCF}\left(s\right) = \left(k_{P_1} + k_{I_1}s^{-\lambda_1} + k_D s^{\mu}\right)\left(k_{P_2} + k_{I_2}s^{-\lambda_2}\right) \tag{20}$$

To back up the efficacy of the proposed FOPID-C-FOPI controller, its performance is compared with that of another proposed FOPID-P-FOPI controller, whose transfer function is detailed in Eq. (21) and depicted in Fig. 8, as well as with traditional FOPID and PID controllers.

$$G_{FPF}(s) = \left(k_{P_1} + k_{I_1}s^{-\lambda_1} + \mathrm{k}_D s^{\mu}\right) + \left(k_{P_2} + k_{I_2}s^{-\lambda_2}\right) \tag{21}$$

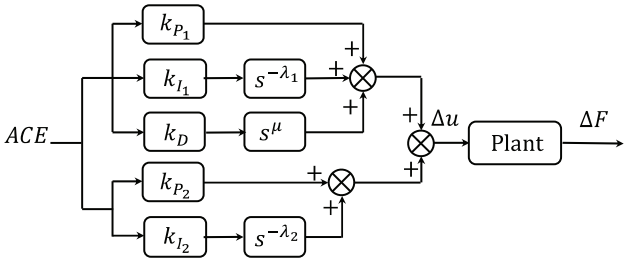

Figure 8: FOPID parallel FOPI

The proposed controllers, acting as mutual backup and employing fractional calculus and a superimposed structure, offer greater flexibility compared to traditional FOPID and PID controllers. Nevertheless, parameter tuning for FOPID presents significant challenges, which can be effectively addressed using the HBO algorithm.

3.3 Parameters Optimization

The recently introduced HBO algorithm harnesses a hierarchical rank structure to update population positions based on interactions among various corporate ranks, as detailed in [22]. Fig. 9a illustrates this concept through a corporate rank hierarchy (CRH), where the chief executive officer (CEO) holds the top position as the root node. Reporting directly to the CEO are the chief operating officer (COO) and chief financial officer (CFO), who manage multiple departments. Colleagues in this context are individuals at the same hierarchical level within the organization.

The necessity for meta-heuristics becomes apparent in optimization scenarios involving multiple variables and large search domains, where traditional methods falter due to complexity. The HBO algorithm, a novel meta-heuristic, incorporates the principles of organizational behavior into its strategy. It employs a heap data structure for its non-linear, tree-based organization, typically used in priority queues, to mirror the CRH effectively. Fig. 9b displays a ternary (3-ary) minimum heap, demonstrating how CRH is represented within the algorithm. This structure aids in organizing

solutions by their fitness values, thus enabling efficient position updates within the algorithm. HBO uniquely integrates three types of employee interactions: between subordinates and their direct bosses, among peers, and individual efforts toward the optimization process, enhancing the algorithm's efficacy and applicability to complex problems.

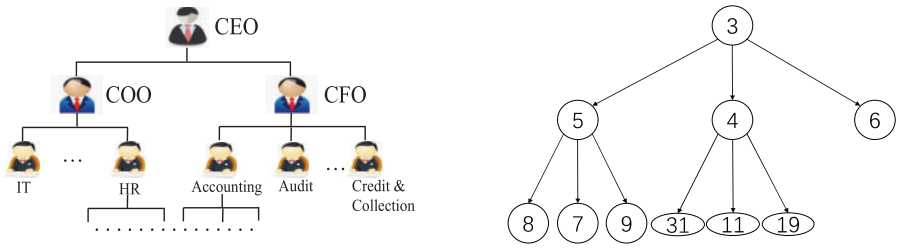

(a) (b)

Figure 9: Examples of corporate rank hierarchy and 3-ary min heap

Fig. 10 illustrates the modeling of CRH using a heap data structure, where x_i denotes the i-th search agent in the population. The figure shows the objective function's landscape, with search agents positioned according to their fitness values. Agents are organized into a heap based on their fitness, where each node's placement reflects its fitness value. For example, x_4 is identified as the optimal solution and is positioned at the heap's root. Notably, min-heaps are utilized for minimization tasks, while max-heaps are appropriate for maximization objectives.

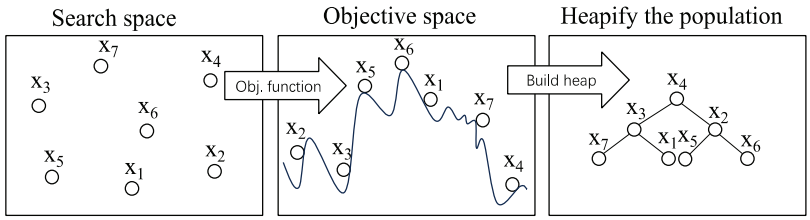

Figure 10: Illustration of the modeling of the CRH with min-heap

The HBO algorithm leverages a ternary tree structure, or minimum heap, to optimize decision-making by utilizing hierarchical connections among agents, including direct supervisors, peers, and intrinsic motivation. The hierarchy is organized with the leader agent, possessing the highest fitness value, at the top, followed by parent agents on the second tier, and the rest agents on the third. The updated dynamics of this structure are detailed in Eq. (22):

$$x_{m,i}^{it+1} = \begin{cases} x_{m,i}^{it}, & r_{m,i} \le r_1 \\ pa_i^{it} + \phi\omega_i \left| pa_i^{it} - x_{m,i}^{it} \right|, & r_1 \le r_{m,i} \le r_2 \\ co_{r,i}^{it} + \phi\omega_i \left| co_{r,i}^{it} - x_{m,i}^{it} \right|, & r_{m,i} > r_2 \cap fit\left(CO_r^{it}\right) < fit\left(X_m^{it}\right) \\ x_{r,i}^{it} + \phi\omega_i \left| co_{r,i}^{it} - x_{m,i}^{it} \right|, & r_{m,i} > r_2 \cap fit\left(CO_r^{it}\right) > fit\left(X_m^{it}\right) \end{cases} \tag{22}$$

where $x_{m,i}^{it}$ represents the i-th component of vector X_m^{it} for the m-th agent in the population following it-th iteration. The fitness of each agent is evaluated using the fitness function $fit(\cdot)$ specified in Eq. (9). The updating of $x_{m,i}^{it}$ is governed by a random probability $r_{m,i}$, which is assessed against thresholds r_1 and r_2, detailed in Eqs. (23) and (24):

$$r_1 = 1 - it/I \tag{23}$$

$$r_2 = r_1 + (1 - r_1)/2 \tag{24}$$

where I represents the total number of iterations, with it denoting the current iteration, the probabilities r_1 and r_2 are recalibrated during each iteration to guide the adjustment process, while $r_{m,i}$ is reproduced for each component update. For $r_{m,i} \leq r_1$, components maintain their current states, reflecting self-motivation, as specified in the first case of Eq. (22). Conversely, for $r_1 \leq r_{m,i} \leq r_2$, updates are made according to the i-th component of the parent node PA^{it} from the current iteration. The influence coefficient ϕ, pivotal in this context, is defined in Eq. (25):

$$\phi = |2 - \mathrm{mod}(it, I/\psi)/[I/(4\psi)]| \tag{25}$$

where mod(x/y) represents a modulus operation, and ψ is computed best as I/25. Throughout the iterative process, ϕ linearly decreases from 2 to 0 and then increases to 2. The parameter ψ is crucial as it determines how many cycles ϕ completes during I iterations. For clarity, two scenarios are illustrated in Fig. 11: in the first, ψ is set to 2, and in the second, to 5, with I consistently at 200. Fig. 11b highlights the potential positions of $\phi\omega_i$ from Eq. (22), which varies depending on the random coefficient ω_i. For example, in the first scenario at iteration 75, $\phi\omega_i$ can range from −1 to 1. In contrast, in the second, it extends from −1.5 to 1.5, demonstrating that ψ significantly influences the fluctuation amplitude of $\phi\omega_i$ as per Eq. (22).

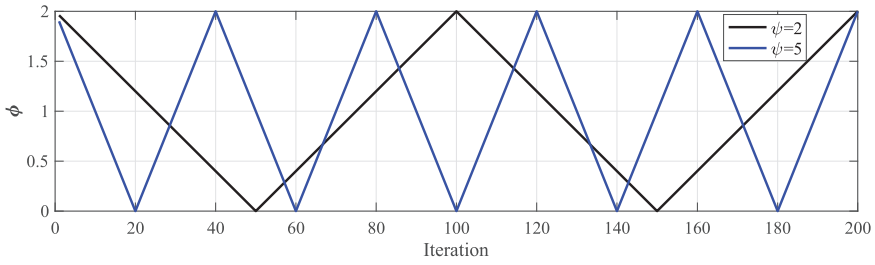

(**a**) **pr**esents two distinct scenarios corresponding to varying values of ψ

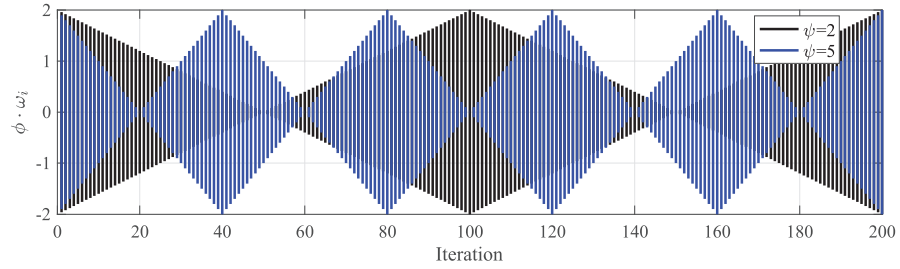

(**b**) delineates the domain where $\phi\omega_i$ from (22) can be located at any position across both scenarios

Figure 11: Visualization of the influence of parameters ψ and I on values of ϕ

In Eq. (22), the second term defines ω_i as the multiplier for the i-th component of X_m, calculated as (2r−1), where r is uniformly distributed between [0, 1]. ω_i is also reproduced for each component update. If $r_{m,i}$ exceeds r_2, the update process concludes, and the model references a peer CO_r^{it} chosen at random, as specified in the third and fourth terms of Eq. (22).

Algorithm 1 illustrates the initialization of the heap structure, and Algorithm 2 details the position updates. Within these algorithms, heap[·].value holds the population index of each agent, while heap[·].key records the agent's fitness. The pseudocode for initializing and updating agents is provided in Algorithms 1 and 2, respectively.

Algorithm 1: Initialize the heap

Input: X (Population of search agents), Q (Population size), $fit_{\mathrm{LD}} = Inf$ (Initial fitness of Leading Position), LD = **0**

for $i = 1{:}1{:}Q$ **do**
  heap[i].value $\leftarrow$ i, heap[i].key $\leftarrow$ fit (X_i)
  while $i > 1$ **do**
    parent(i) $\leftarrow$ floor $((i + 1)/3)$
    if heap[i].key<heap[parent(i)].key **then**
      swap(heap[i], heap[parent(i)]), $i \leftarrow$ parent(i)
    end if
  end while
end for

Algorithm 2: Update the search agent

Input: X (Population of search agents), Q (Population size)
Output: LD, fit_{LD}

for $it = 1 : 1 : I$ **do**
  Compute ϕ Using Eq. (25)
  Compute r_1 and r_2 using Eqs. (23) and (24)
  for $K = Q{:}-1{:}2$ **do**
    $k \leftarrow$heap[K].value
    $pk \leftarrow$heap[parent(K)].value
    $ck \leftarrow$heap[colleague(K)].value
    $PA \leftarrow X_{pk}$, CO $\leftarrow X_{ck}$
    for $i = 1{:}1{:}dim$ **do**
      $r_{m,i} \leftarrow$ rand()
      $x^{it}_{temp,i} \leftarrow x^{it}_{m,i}$ using Eq. (22)
    end for
    if $fit\left(X^{it}_{temp}\right) < fit\left(X^{it}_{m}\right)$
      $X^{it+1}_{m} \leftarrow X^{it}_{temp}$
    end if
    if heap[i].key<heap[parent(i)].key **then**
      swap(heap[i], heap[parent(i)]), $i \leftarrow$ parent(i)
    end if
  end for
end for
Return LD, fit_{LD}

4 Simulation Results and Discussions

Simulations were conducted using MATLAB to analyze a system consisting of two interconnected AC MGs, with MG 1 experiencing all load and renewable generation fluctuations (see Fig. 1). Detailed system parameters and constraints on ramp rates and power output are listed in the Appendix A [28,29,35].

Fig. 12 illustrates wind speed and solar irradiation variations, with a constant wind speed of 5 m/s superimposed with white noise, resulting in a power spectral density (PSD) of 0.02, depicted by the black line. Wind power variations due to this noise are shown in blue. Additionally, fluctuations in solar irradiation and the corresponding PV power output variation are represented by pink and red lines in Fig. 12.

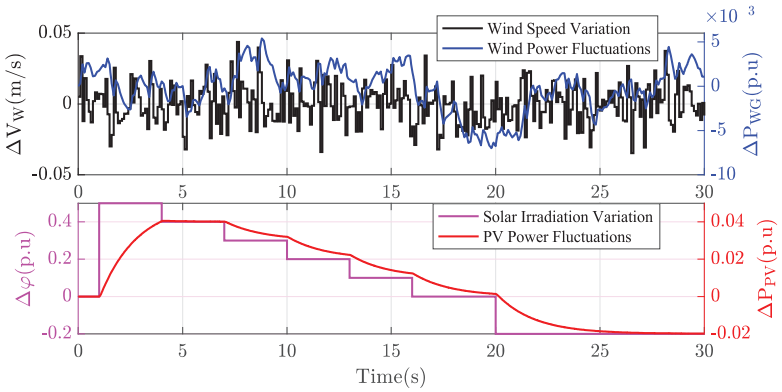

Figure 12: Power changing patterns of WG and PV

4.1 Validation of the Proposed Structures of the Controllers

The efficacy of the FOPID-C-FOPI controller is systematically validated by benchmarking its response against traditional FOPID [14], PID [21], and alternative FOPID-P-FOPI controllers across two distinct scenarios. For this analysis, it is presumed that only load step changes impact the system, with the output from PV and WG held constant ($\Delta\gamma = 0$ and $\Delta v = 0$).

Scenario 1 involves a 0.1 p.u. step increase in load within MG 1 (as depicted in Fig. 1), termed step load augmentation (SLA). For this scenario, the tuning ranges for the proportional (k_P), integral (k_I), and derivative (k_D) gains of the FOPID-based controllers are set between [0, 5], with their fractional orders λ and μ constrained within [0, 2]. In contrast, the PID controller's gains are bounded [−5, 5].

Parameter optimization for all controllers employs the HBO method, maintaining consistency in population size and iteration limits across evaluations. The dynamic responses for this scenario, alongside the comparative fitness values of the controllers through iterative adjustments, are illustrated in Figs. 13, 14 and Table 1.

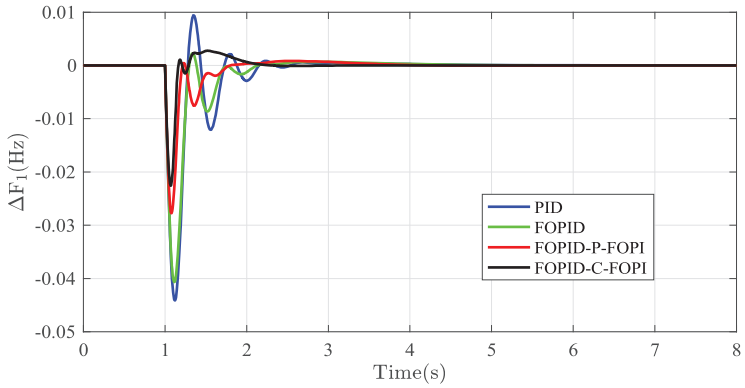

(**a**) ΔF_1 variation in MG 1

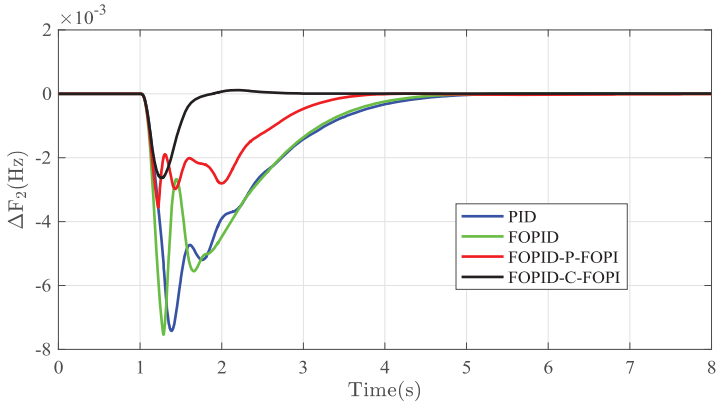

(**b**) ΔF_2 variation in MG 2

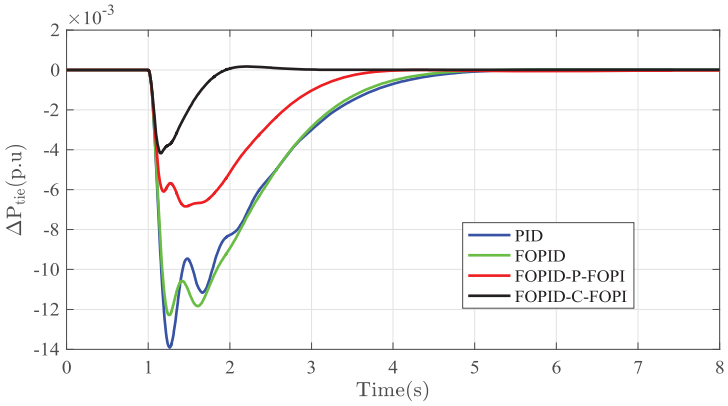

(**c**) ΔP_{tie} variation

Figure 13: Responses of the interconnected MGs based on SLA under different controllers

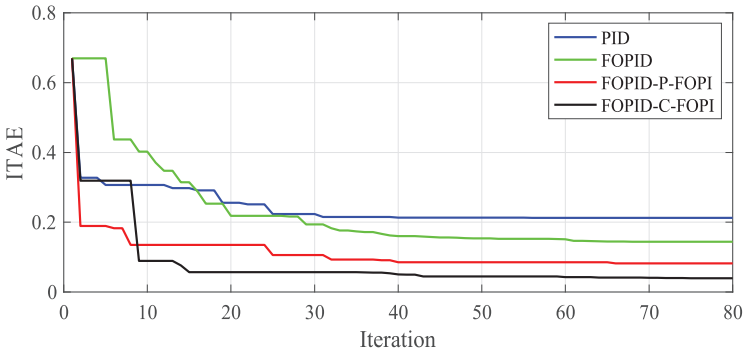

Figure 14: Fitness values of four controllers

Table 1: ITAE of each controller in Scenarios 1, 2

	PID	FOPID	FOPID-P-FOPI	FOPID-C-FOPI
Scenario 1	0.061	0.055	0.030	0.012
Scenario 2	1.632	1.489	0.809	0.184

In Scenario 1, the FOPID-C-FOPI and FOPID-P-FOPI controllers significantly outperform traditional PID and FOPID controllers in reducing frequency and tie-line power fluctuations across MGs despite all being optimized via the same HBO algorithm. The FOPID-C-FOPI controller reduces F_1 reduction by up to 48.8% compared to PID, demonstrating superior control efficacy, while the FOPID-P-FOPI controller performs the lowest ΔF_1 overshoot. This performance superiority extends to ΔF_2 and tie-line power variance, with FOPID-C-FOPI showing flatter and faster convergence profiles.

When optimized using the HBO algorithm, the FOPID-C-FOPI and FOPID-P-FOPI controllers demonstrate leading and second performance compared to the PID, FOPID, and FOPID-P-FOPI controllers, as evidenced in Fig. 14. Despite having 16 parameters to tune (denoted as n_v), the 14th iteration achieves the optimal configuration for the FOPID-C-FOPI controller. In contrast, the optimal parameters for the PID, FOPID, and FOPID-P-FOPI controllers, requiring tuning of 6, 10, and 16 parameters, respectively, are realized around the 30th iteration, while the FOPID-P-FOPI controller shows the suboptimal performance among these controllers.

Scenario 2 involves multiple-step load perturbations in MG 1, denoted as MSLP. The corresponding load fluctuations, ΔP_L, in MG 1 are depicted in Fig. 15 and quantified in Eq. (26):

$$\begin{aligned}\Delta \mathrm{P_L} =& 0.02u\,(t-1) + 0.02u\,(t-11) - 0.04u\,(t-21) + 0.03u\,(t-31) + 0.01u\,(t-41) \\ & - 0.02u\,(t-51) - 0.02u\,(t-61) \end{aligned} \tag{26}$$

where $u(t)$ represents the unit step function. For this scenario, the controller parameters for FOPID, FOPID-P-FOPI, and FOPID-C-FOPI range from [0, 5] for k_P, k_I, and k_D, and [0, 2] for λ and μ; PID controller parameters vary within [−5, 5]. The optimization process involves a population size of 23 and a maximum of 80 iterations.

Dynamic responses, depicted in Fig. 16 and Table 1, demonstrate that all controllers effectively manage the load perturbation. The most significant disturbance occurs at $t = 21$ s, with $\Delta P_L = -0.04$

p.u. Fig. 16a,b highlights the frequency deviations ΔF_1 and ΔF_2, showcasing superior performance by the FOPID-C-FOPI and FOPID-P-FOPI. The controllers achieve a peak overshoot of less than 0.01 Hz for ΔF_1, compared to over 0.01 Hz with PID and FOPID, and less than 0.0012 Hz for ΔF_2, *vs*. more than 0.0015 Hz with the alternatives. Fig. 16c illustrates the tie-line power variance, where the FOPID-C-FOPI and FOPID-P-FOPI exhibit lower fluctuation and faster stabilization than the other controllers.

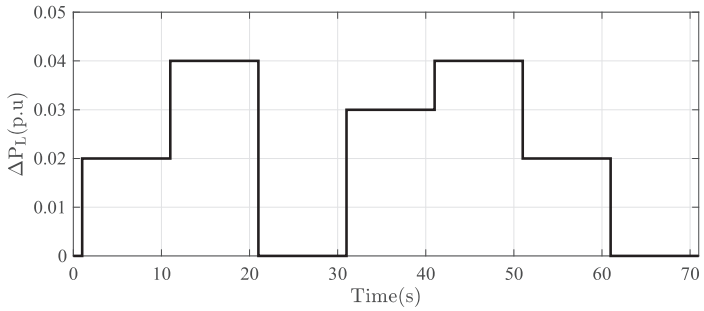

Figure 15: ΔP_L variation in MG 1

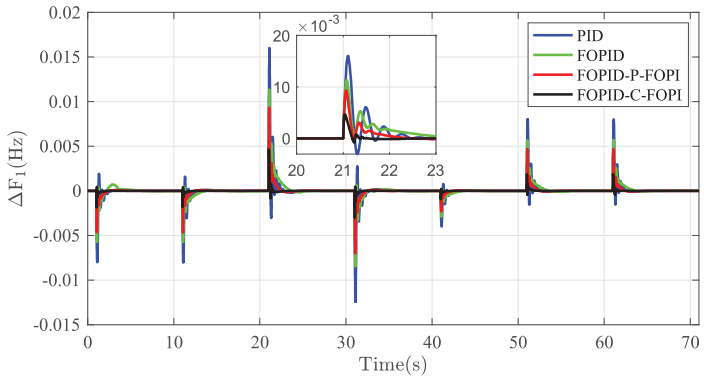

(**a**) ΔF_1 variation in MG 1

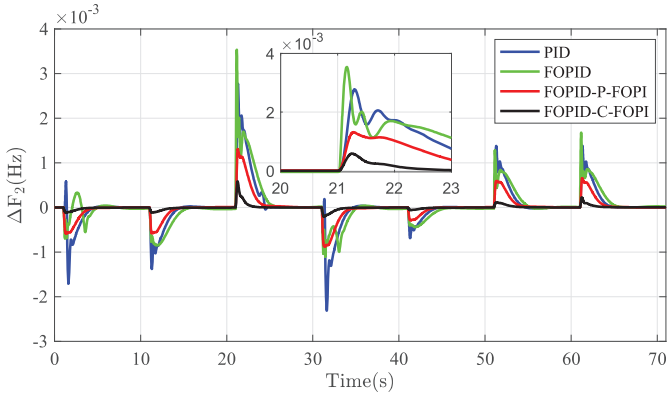

(**b**) ΔF_2 variation in MG 2

Figure 16: (Continued)

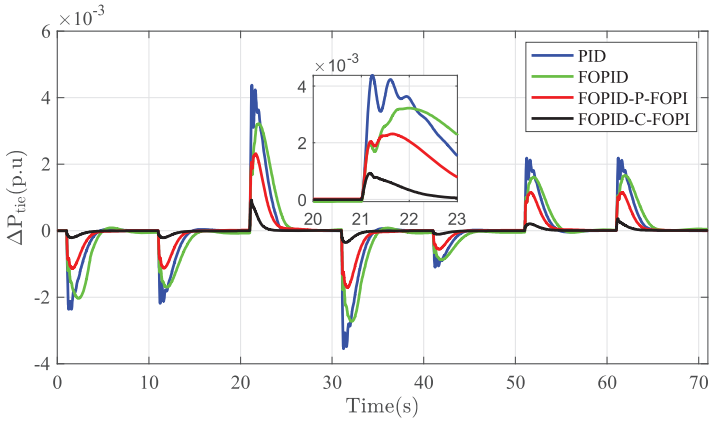

(c) ΔP_{tie} variation

Figure 16: Responses of the interconnected MGs based on MSLP

4.2 Validation of the Optimal Parameters Search

In this study, the FOPID-C-FOPI and FOPID-P-FOPI controllers involve optimizing 16 parameters, denoted as $n_v = 16$. In this subsection, we only consider the parameters selection of FOPID-C-FOPI controller.

The parameters are optimized using meta-heuristic algorithms, with the HBO method being the primary approach, benchmarked against particle swarm optimization (PSO), whale optimization algorithm (WOA) [36], and grey wolf optimizer (GWO) [37], hybrid grey wolf optimizer particle swarm optimization (HGWOPSO) [38]. Prior to Scenario 3, HBO is utilized to manage a case involving a 0.2 p.u. step load increase in MG 1, referred to as SLA. Fig. 14 demonstrates HBO's effectiveness in parameter optimization, showcasing its convergent behavior across multiple controller configurations. This paper will subsequently compare the performance of HBO with other prevalent optimization algorithms.

Scenario 3 involves a 0.03 p.u. step load increase in MG 1 (see Fig. 1). For the FOPID-C-FOPI controllers, the parameters k_P, k_I, and k_D are constrained within [0, 5], while λ and μ are restricted to [0, 2]. Consistent hyper-parameters across the algorithms include a population size of 23 and a maximum of 80 iterations. The parameter ψ, detailed in Section 3.3, is set at 3. This scenario is utilized to evaluate the superiority of HBO against other heuristic algorithms, and the same initial parameters are set for each algorithm. The HBO algorithm demonstrates superior performance relative to other algorithms, as evidenced in Fig. 17, achieving the optimal solution within 20 iterations.

4.3 Robustness Evaluation of the HBO-Based Controllers

This section assesses the robustness of the HBO-based FOPID-C-FOPI and FOPID-P-FOPI against system uncertainties, investigated in Scenarios 4–6. The original parameters of the MG 1 and MG 2 are described in Appendix A. In this subsection, the system perturbation is set as the power output fluctuations of WG, specifically under conditions where $\Delta\gamma = 0$ or $\Delta v \neq 0$. With the output power reduction (in Fig. 18) of WG reaching 0.2 p.u. between 1 s and 10 s with wind speed noise described in Fig. 12, Scenario 4–6 are defined as follows:

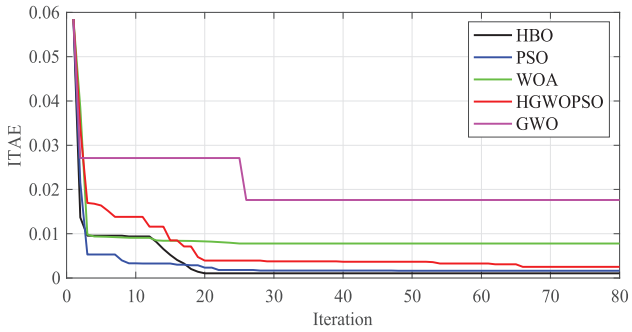

Figure 17: Performance of each algorithm for the FOPID-C-FOPI

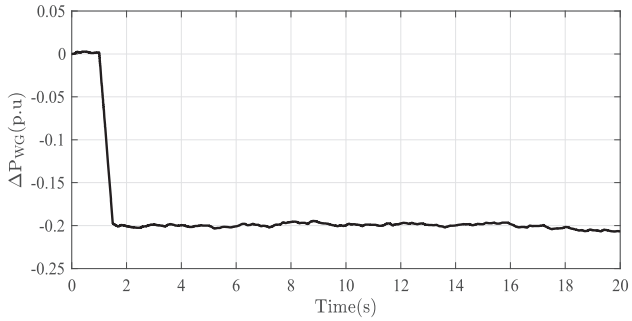

Figure 18: ΔP_{WG} reduction in MG 1

Scenario 4 investigates a system of the interconnected MGs with inter-area synchronous torque coefficient $T_{12}^{'} = 2T_{12}$.

Scenario 5 investigates the same situation except for $T_{12}^{'} = 0.5T_{12}$.

Scenario 6 investigates a system with comprehensive parameter changes compared to the original system, as $\beta_1^{'} = 0.75\beta_1$, $\beta_2^{'} = 0.75\beta_2$, $D_1^{'} = 0.75D_1$, $D_2^{'} = 0.75D_2$, $T_g^{'} = 1.25T_g$, $T_{tg}^{'} = 1.25T_{tg}$, $H_1^{'} = 1.25H_1$, $H_2^{'} = 1.25H_2$.

The performance outcomes in Scenario 4, illustrated across Fig. 19a–c and Table 2, are designed to assess controller robustness under $T_{12}^{'} = 2T_{12}$ with 0.2 p.u. WG output reduction and wind speed noise. Both the frequency and tie-line power deviations, ΔF_1, ΔF_2, and ΔP_{tie}, exhibit reduced drop and overshoot with the proposed controllers compared to others. Responses to a decrease in WG output containing noise highlight the PID controller's underperformance and obvious oscillatory response, primarily due to its restricted parameter tuning capabilities, whereas the FOPID-C-FOPI and FOPID-P-FOPI maintain the most stable response. Notably, FOPID-C-FOPI consistently exhibits minimal fluctuations in ΔF_2 and ΔP_{tie}, underscoring its advantage stemming from a more extensive parameter set.

The results of Scenario 5 are illustrated in Fig. 20 and Table 2, which displays comparable performance to Scenario 4, where the ΔF_2 performance of the FOPID-P-FOPI controller marginally outperforms the FOPID-C-FOPI with a miner overshoot.

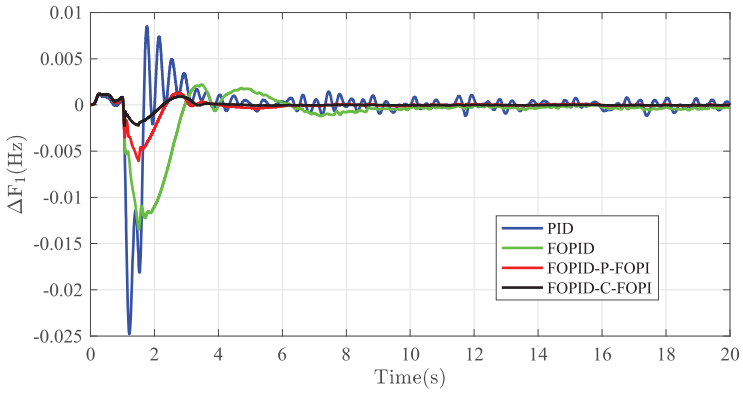

(**a**) ΔF_1 variation in MG 1

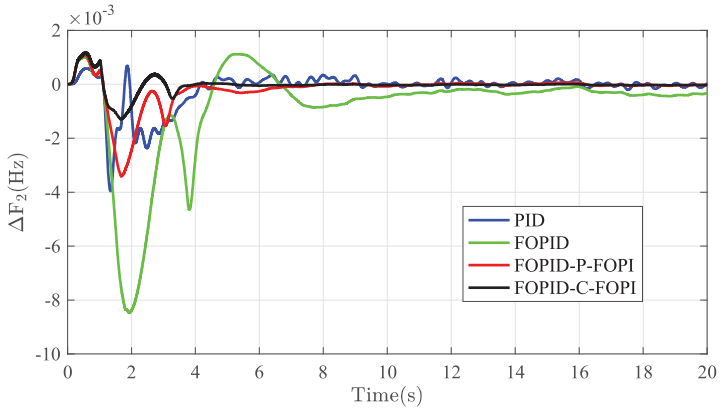

(**b**) ΔF_2 variation in MG 2

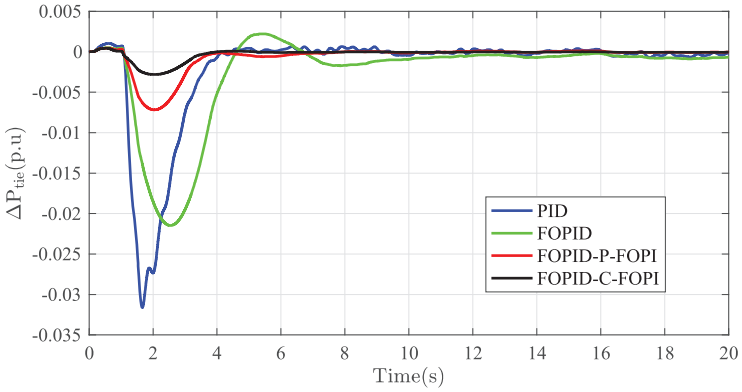

(**c**) ΔP_{tie} variation

Figure 19: Responses of the interconnected MGs based on WG sudden decrease containing noise with $2T_{12}$

Table 2: ITAE of Scenarios 4, 5

	PID	FOPID	FOPID-P-FOPI	FOPID-C-FOPI
Scenario 4	0.217	0.264	0.053	0.023
Scenario 5	0.365	0.197	0.079	0.046
Scenario 6	0.290	0.295	0.051	0.033

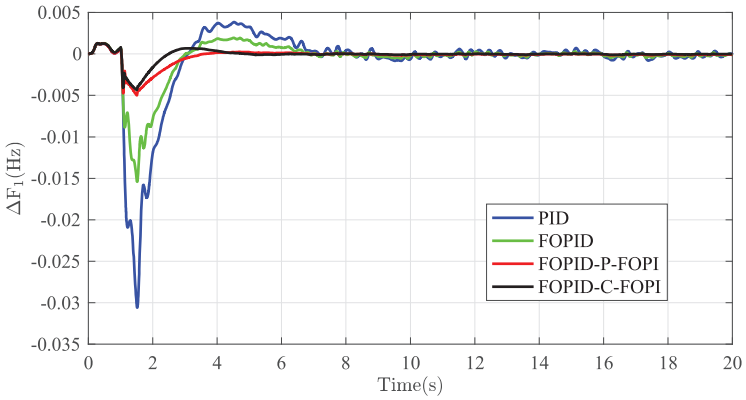

(**a**) ΔF_1 variation in MG 1

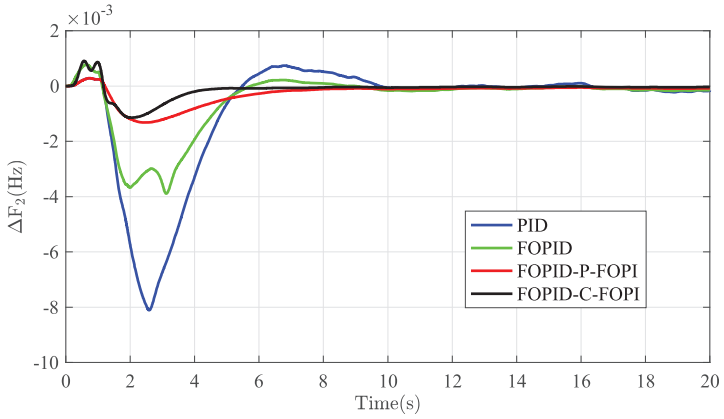

(**b**) ΔF_2 variation in MG 2

Figure 20: (Continued)

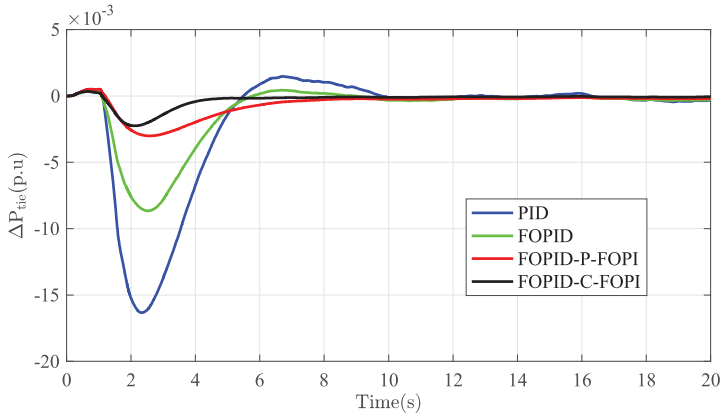

(**c**) ΔP_{tie} variation

Figure 20: Responses of the interconnected MGs based on WG sudden decrease containing noise with $0.5T_{12}$

Further, the performance in Scenario 6, with multiple parameters tuned, shows strong robustness against system parameter changes with both FOPID-P-FOPI and FOPID-C-FOPI controllers in Fig. 21 and Table 2. The oscillation happens after load reduction with noise for PID and FOPID controllers.

Figs. 19–21 illustrate that ΔF_1, ΔF_2, and ΔP_{tie} swiftly adjust to power fluctuations with FOPID-P-FOPI and FOPID-C-FOPI controllers, achieving steady-state values under system uncertainties. The simulation results affirm the superior capability of the FOPID-C-FOPI controller in managing system perturbations, highlighting its robustness and effectiveness in stabilizing the interconnected system under variable conditions. This performance is enhanced by the HBO-based control strategy. Furthermore, the FOPID-C-FOPI and FOPID-P-FOPI controllers effectively maintain frequency variations within the [−0.2, 0.2] per unit range, aligning with the Chinese regulatory standards [39]. This positions the FOPID-P-FOPI controller as a viable supplementary or backup option to the FOPID-C-FOPI controller.

4.4 Discussions

The efficacy of the heap-based optimization (HBO) in selecting the controller parameters outweighs other traditional and novel heuristic-based optimization method, manifesting in convergency speed and error of ITAE. The robustness of the proposed back-up controllers demonstrates the system reliability for both frequency and tie-line power deviations. Scenarios 4–6 investigate the system responses under different interconnected microgrids systems with $T_{12}^{'} = 2T_{12}$ (Scenario 4), $T_{12}^{'} = 0.5T_{12}$ (Scenario 5), and $\beta_1^{'} = 0.75\beta_1$, $\beta_2^{'} = 0.75\beta_2$, $D_1^{'} = 0.75D_1$, $D_2^{'} = 0.75D_2$, $T_g^{'} = 1.25T_g$, $T_{tg}^{'} = 1.25T_{tg}$, $H_1^{'} = 1.25H_1$, $H_2^{'} = 1.25H_2$ (Scenario 6), respectively. It is evident that the two back-up controllers perform better than simple PID and FOPID controllers optimized using HBO-based method while encountering the system parameter changes.

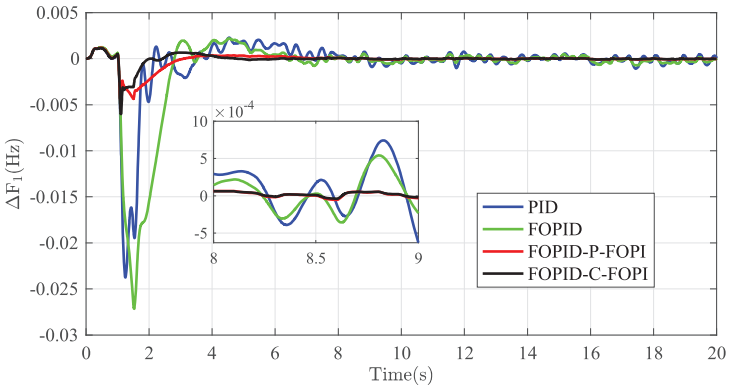

(**a**) ΔF_1 variation in MG 1

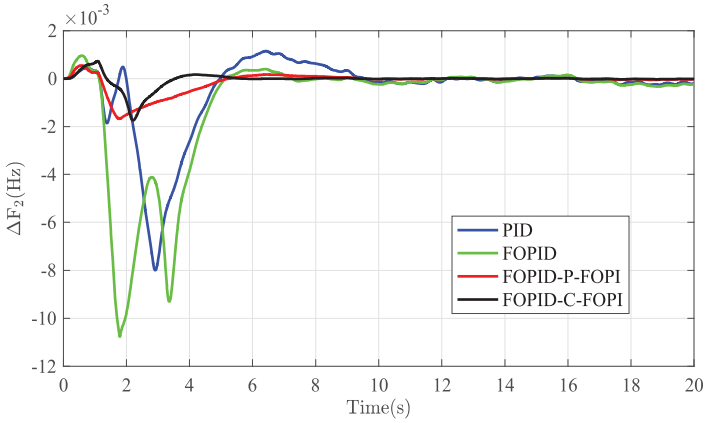

(**b**) ΔF_2 variation in MG 2

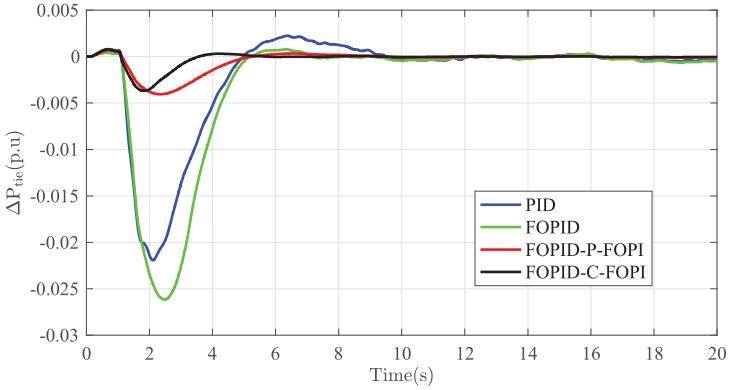

(**c**) ΔP_{tie} variation

Figure 21: Responses of interconnected MGs based on WG sudden decrease containing noise with comprehensive power parameter changes

5 Conclusion

This study substantiates the effectiveness of innovative dual-backup fractional order proportional integral derivative (FOPID) controllers, FOPID cascaded with fractional-order PI (FOPID-C-FOPI) and FOPID parallel fractional-order PI (FOPID-P-FOPI), in fortifying frequency and tie-line power stability within microgrids, particularly in the context of escalating renewable energy integration. Implemented within a two-area interconnected microgrid system, these controllers significantly outperform traditional PID and FOPID systems in managing dynamic fluctuations and disturbances. Comparative analyses confirm these advanced controllers' superior performance and robustness, further enhanced by an optimization algorithm that surpasses conventional artificial intelligence methods in efficiency and precision. Adopting a dual-controller scheme boosts system resilience and ensures operational continuity through mutual backup functionality. This research highlights the critical role of advanced control mechanisms in adapting microgrid operations to the rapidly evolving energy sector, providing reliability and stability amidst diverse and intermittent energy inputs. Future studies will focus on expanding the scope to include simultaneous disturbances in multiple microgrids and exploring the responsive characteristics of flexible load consumers.

Acknowledgement: None.

Funding Statement: The authors received no specific funding for this study.

Author Contributions: The authors confirm contribution to the paper as follows: study conception and design: Aijia Ding; data collection: Aijia Ding; analysis and interpretation of results: Aijia Ding and Tingzhang Liu; draft manuscript preparation: Aijia Ding. All authors reviewed the results and approved the final version of the manuscript.

Availability of Data and Materials: Data sharing is not applicable to this article as no datasets were generated or analyzed during the current study.

Ethics Approval: Not applicable.

Conflicts of Interest: The authors declare that they have no conflicts of interest to report regarding the present study.

References

[1] G. Magdy, E. A. Mohamed, G. Shabib, A. A. Elbaset, and Y. Mitani, "Microgrid dynamic security considering high penetration of renewable energy," *Prot. Contr. Mod. Pow.*, vol. 3, no. 1, pp. 1–11, Jul. 2018. doi: 10.1186/s41601-018-0093-1.

[2] H. H. Alhelou, P. Siano, M. Tipaldi, R. Ier-volino, and F. Mahfoud, "Primary frequency response improvement in interconnected power systems using electric vehicle virtual power plants," *World Electr. Veh. J.*, vol. 11, no. 2, May 2020, Art. no. 40. doi: 10.3390/wevj11020040.

[3] S. Kumari and G. Shankar, "Novel application of integral-tilt-derivative controller for performance evaluation of load frequency control of interconnected power system," *IET Gener. Transm. Dis.*, vol. 12, no. 14, pp. 3550–3560, Jun. 2018. doi: 10.1049/iet-gtd.2018.0345.

[4] M. Ahmed, G. Magdy, M. Khamies, and S. Kamel, "Modified TID controller for load frequency control of a two-area inter-connected diverse-unit power system," *Int. J. Elec. Power*, vol. 135, Feb. 2022, Art. no. 107528. doi: 10.1016/j.ijepes.2021.107528.

[5] L. Dritsas, E. Kontouras, E. Vlahakis, I. Kitsios, G. Halikias and A. Tzes, "Modelling issues and aggressive robust load frequency control of interconnected electric power systems," *Int. J. Control*, vol. 95, no. 3, pp. 753–767, Sep. 2022. doi: 10.1080/00207179.2020.1821248.

[6] G. K. Suman, J. M. Guerrero, and O. P. Roy, "Robust frequency control in interconnected microgrids: An H_2/H_∞ control approach," *IEEE Syst. J.*, vol. 16, no. 2, pp. 2044–2055, Sep. 2021. doi: 10.1109/JSYST.2021.3108685.

[7] D. Yanget *et al*., "Inertia-adaptive model predictive control-based load frequency control for interconnected power systems with wind power," *IET Gener. Transm. Dis.*, vol. 14, no. 22, pp. 5029–5036, Jul. 2020. doi: 10.1049/iet-gtd.2020.0018.

[8] M. H. Fini and M. E. H. Golshan, "Determining optimal virtual inertia and frequency control parameters to preserve the frequency stability in islanded microgrids with high penetration of renewables," *Electr. Pow. Syst. Res.*, vol. 154, pp. 13–22, Jan. 2018. doi: 10.1016/j.epsr.2017.08.007.

[9] Y. Arya, "Effect of electric vehicles on load frequency control in interconnected thermal and hydrothermal power systems utilizing CF-FOIDF controller," *IET Gener. Transm. Dis.*, vol. 14, no. 14, pp. 2666–2675, May 2020. doi: 10.1049/iet-gtd.2019.1217.

[10] E. Çelik, N. Öztürk, Y. Arya, and C. Ocak, "(1 + PD)-PID cascade controller design for performance betterment of load frequency control in diverse electric power systems," *Neural Comput. Appl.*, vol. 33, no. 22, pp. 15433–15456, Nov. 2021. doi: 10.1007/s00521-021-06168-3.

[11] D. Murugesan, K. Jagatheesan, P. Shah, and R. Sekhar, "Fractional order $PI^{\lambda}D^{\mu}$ controller for microgrid power system using cohort intelligence optimization," *Res. Control Optim.*, vol. 11, Jun. 2023, Art. no. 100218. doi: 10.1016/j.rico.2023.100218.

[12] H. Abubakr, T. H. Mohamed, M. M. Hussein, J. M. Guerrero, and G. Agundis-Tinajero, "Adaptive frequency regulation strategy in multi-area microgrids including renewable energy and electric vehicles supported by virtual inertia," *Int. J. Elec. Power*, vol. 129, Jul. 2021, Art. no. 106814. doi: 10.1016/j.ijepes.2021.106814.

[13] S. Oshnoei, M. R. Aghamohammadi, S. Oshnoei, S. Sahoo, A. Fathollahi and M. H. Khooban, "A novel virtual inertia control strategy for frequency regulation of islanded microgrid using two-layer multiple model predictive control," *Appl. Energ.*, vol. 343, Aug. 2023, Art. no. 121233. doi: 10.1016/j.apenergy.2023.121233.

[14] S. Sondhi and Y. V. Hote, "Fractional order PID controller for load frequency control," *Energ. Convers. Manage.*, vol. 85, pp. 343–353, Sep. 2014. doi: 10.1016/j.enconman.2014.05.091.

[15] E. M. Ahmed *et al*., "Improving load frequency control performance in interconnected power systems with a new optimal high degree of freedom cascaded FOTPID-TIDF controller," *Ain Shams Eng. J.*, vol. 14, no. 10, Oct. 2023, Art. no. 102207. doi: 10.1016/j.asej.2023.102207.

[16] M. Bhuyan, D. C. Das, and A. K. Barik, "Chaotic butterfly optimization algorithm based cascaded PI-TID controller for frequency control in three area hybrid microgrid system," *Optim. Contr. Appl. Met.*, vol. 44, no. 5, pp. 2595–2619, Mar. 2023. doi: 10.1002/oca.2994.

[17] M. Bhuyan, D. C. Das, and A. K. Barik, "Proficient power control strategy for combined solar gas turbine-wind turbine generator-biodiesel generator based two area interconnected microgrid employed with DC link using Harris's hawk optimization optimised tilt-integral-derivative controller," *Int. J. Numer. Model. El.*, vol. 35, no. 4, Feb. 2022, Art. no. e2991. doi: 10.1002/jnm.2991.

[18] A. Latif, S. M. S. Hussain, D. C. Das, and T. S. Ustun, "State-of-the-art of controllers and soft computing techniques for regulated load frequency management of single/multi-area traditional and renewable energy-based power systems," *Appl. Energ.*, vol. 266, May 2020, Art. no. 114858. doi: 10.1016/j.apenergy.2020.114858.

[19] S. Sondhi and Y. V. Hote, "Fractional order PID controller for perturbed load frequency control using kharitonov's theorem," *Int. J. Elec. Power*, vol. 78, pp. 884–896, Jun. 2016. doi: 10.1016/j.ijepes.2015.11.103.

[20] A. Zamani, S. M. Barakati, and S. Yousofi-Darmian, "Design of a fractional order pid controller using gbmo algorithm for load-frequency control with governor saturation consideration," *ISA Trans.*, vol. 64, pp. 56–66, Sep. 2016. doi: 10.1016/j.isatra.2016.04.021.

[21] B. Kumar and S. Bhongade, "Load disturbance rejection based pid controller for frequency regulation of a microgrid," in *Proc. PESTSE*, Bengaluru, India, Jul. 2016, pp. 1–6. doi: 10.1109/PESTSE.2016.7516459.

[22] Q. Askari, M. Saeed, and I. Younas, "Heap-based optimizer inspired by corporate rank hierarchy for global optimization," *Expert Syst. Appl.*, vol. 161, Dec. 2020, Art. no. 113702. doi: 10.1016/j.eswa.2020.113702.

[23] G. K. Suman and O. P. Roy, "Microgrid system for a rural area-an analysis of homer optimised model using MATLAB," in *Proc. RDCAPE*, Noida, India, 2019, pp. 534–539. doi: 10.1109/RDCAPE47089.2019.8979097.

[24] D. Lee and L. Wang, "Small-signal stability analysis of an autonomous hybrid renewable energy power generation/energy storage system part I: Time-domain simulations," *IEEE Trans. Energy Conver.*, vol. 23, no. 1, pp. 311–320, Feb. 2008. doi: 10.1109/TEC.2007.914309.

[25] M. H. Khooban and M. Gheisarnejad, "A novel deep reinforcement learning controller based type-II fuzzy system: Frequency regulation in microgrids," *IEEE Trans. Emerg. Top. Comput. Intell.*, vol. 5, no. 4, pp. 689–699, Jan. 2020. doi: 10.1109/TETCI.2020.2964886.

[26] Y. Wang, Z. Sun, X. Li, X. Yang, and Z. Chen, "A comparative study of power allocation strategies used in fuel cell and ultracapacitor hybrid systems," *Energy*, vol. 189, Dec. 2019, Art. no. 116142. doi: 10.1016/j.energy.2019.116142.

[27] A. Abazari, H. Monsef, and B. Wu, "Coordination strategies of distributed energy resources including FESS, DEG, FC and WTG in load frequency control (LFC) scheme of hybrid isolated micro-grid," *Int. J. Elec. Power*, vol. 109, pp. 535–547, Jul. 2019. doi: 10.1016/j.ijepes.2019.02.029.

[28] M. I. Ibraheem, M. Edrisi, M. Gholipour, and H. H. Alhelou, "A novel frequency regulation in islanded microgrid using sliding mode control with disturbance observers considering storages and EVs," *Comput. Electr. Eng.*, vol. 105, Jan. 2023, Art. no. 108537. doi: 10.1016/j.compeleceng.2022.108537.

[29] P. Indranil and S. Das, "Kriging based surrogate modeling for fractional order control of microgrids," *IEEE Trans. Smart Grid*, vol. 6, no. 1, pp. 36–44, Jul. 2014. doi: 10.1109/TSG.2014.2336771.

[30] H. Bevrani, F. Habibi, P. Babahajyani, M. Watanabe, and Y. Mitani, "Intelligent frequency control in an ac microgrid: Online pso-based fuzzy tuning approach," *IEEE Trans. Smart Grid*, vol. 3, no. 4, pp. 1935–1944, Jun. 2012. doi: 10.1109/TSG.2012.2196806.

[31] S. Mokhtar and A. M. Alsseid, "Cascade of fractional order PID based PSO algorithm for LFC in two-area power system," in *Proc. ICERA*, Yogyakarta, Indonesia, 2021, pp. 1–6. doi: 10.1109/ICERA53111.2021.9538646.

[32] M. Javad, K. Zare, and M. T. Hagh, "Applying fractional order PID to design TCSC-based damping controller in coordination with automatic generation control of interconnected multi-source power system," *Eng. Sci. Technol.*, vol. 20, no. 1, pp. 1–17, Feb. 2017. doi: 10.1016/j.jestch.2016.06.002.

[33] I. Pan and S. Das, "Chaotic multi-objective optimization based design of fractional order $PI^{\lambda}D^{\mu}$ controller in AVR system," *Int. J. Electr. Power*, vol. 43, no. 1, Dec. 2012, Art. no. 393407. doi: 10.1016/j.ijepes.2012.06.034.

[34] S. Debbarma, L. C. Saikia, and N. Sinha, "AGC of a multi-area thermal system under deregulated environment using a non-integer controller," *Electr. Pow. Syst. Res.*, vol. 95, pp. 175–183, Feb. 2013. doi: 10.1016/j.epsr.2012.09.008.

[35] J. C. Vinitha, G. Ramadas, and P. U. Rani, "PSO based fuzzy logic controller for load frequency control in EV charging station," *J. Electr. Eng. Technol.*, vol. 19, no. 1, pp. 193–208, Jul. 2023. doi: 10.1007/s42835-023-01568-y.

[36] P. C. Sahu, R. C. Prusty, and S. Panda, "Frequency regulation of an electric vehicle-operated micro-grid under WOA-tuned fuzzy cascade controller," *Int. J. Ambient Energy*, vol. 43, no. 1, pp. 2900–2911, 2022. doi: 10.1080/01430750.2020.1783358.

[37] B. Kumar, S. Adhikari, S. Datta, and N. Sinha, "Real time simulation for load frequency control of multisource microgrid system using grey wolf optimization based modified bias coefficient diagram method (GWO-MBCDM) controller," *J. Electr. Eng. Technol.*, vol. 16, no. 1, pp. 205–221, Nov. 2020. doi: 10.1007/s42835-020-00596-2.

[38] M. A. Shaheen, H. M. Hasanien, and A. Alkuhayli, "A novel hybrid GWO-PSO optimization technique for optimal reactive power dispatch problem solution," *Ain Shams Eng. J.*, vol. 12, no. 1, pp. 621–630, Mar. 2021. doi: 10.1016/j.asej.2020.07.011.

[39] Y. Pan, X. Liu, W. J. Zhu, and H. X. Lin, *Power Quality-Frequency Deviation for Power System*. Beijing, China: China Standards Press, 2008.

Appendix A

Table A1: Parameters of the system

H_1/H_2	0.0833	R_{DsG}	3	T_{12}	0.318	T_{ic}	0.004	μ_g	0.45	δ_g	0.5
D_1/D_2	0.015	T_g	0.08	T_{fc}	0.26	T_{pv}	1.8	μ_b/μ_{fw}	0.11	δ_b/δ_{fw}	0.05
β_1/β_2	0.3846	T_{Tg}	0.4	T_{in}	0.04	T_b/T_{fw}	0.1	μ_{fc}	0.48	δ_{fc}	1